nature geoscience

ARTICLES

PUBLISHED ONLINE: 26 DECEMBER 2016 | DOI: 10.1038/NGEO2864

Supercycle at the Ecuadorian subduction zone revealed after the 2016 Pedernales earthquake

J.-M. Nocquet[1]*, P. Jarrin[2], M. Vallée[3], P. A. Mothes[2], R. Grandin[3], F. Rolandone[1,4], B. Delouis[1], H. Yepes[2], Y. Font[1], D. Fuentes[2], M. Régnier[1], A. Laurendeau[2], D. Cisneros[5], S. Hernandez[2], A. Sladen[1], J.-C. Singaucho[2], H. Mora[6], J. Gomez[5], L. Montes[5] and P. Charvis[1]

Large earthquakes are usually assumed to release all of the strain accumulated since the previous event, implying a reduced seismic hazard after them. However, long records of seismic history at several subduction zones suggest supercycle behaviour, where centuries-long accumulated strain is released through clustered large earthquakes, resulting in an extended period of enhanced seismic hazard. Here we combine historical seismology results, present-day geodesy data, and dense local observations of the recent M_w 7.8 2016 Pedernales earthquake to reconstruct the strain budget at the Ecuador subduction zone since the great 1906 earthquake. We show that the Pedernales earthquake involved the successive rupture of two patches on the plate interface that were locked prior to the earthquake and most probably overlaps the area already ruptured in 1942 by a similar earthquake. However, we find that coseismic slip in 2016 exceeds the deficit accumulated since 1942. The seismic moment of every large earthquake during the twentieth century further exceeds the moment deficit accumulated since 1906. These results, together with the seismic quiescence before 1906 highlighted by historical records and marine palaeoseismology, argue for an earthquake supercycle at the Ecuador–Colombia margin. This behaviour, which has led to an enhanced seismic hazard for 110 years, is possibly still going on and may apply to other subduction zones that recently experienced a great earthquake.

During the twentieth century, the Ecuador–Colombia subduction zone hosted one of the largest seismic sequences ever recorded by seismometers[1–5]. The sequence started with the great 1906 M_w 8.5–8.8 earthquake[2,6–8], which ruptured a ~500-km-long segment of the megathrust from northern Ecuador to south of Buenaventura (latitude 3.9° N) in Colombia[1,2]. During the following decades, three large earthquakes (M_w 7.7–8.2)[2–5] broke again several sub-segments within the same area, sequentially from south to north (Fig. 1). The 2016 Pedernales earthquake appears to mark a new step of the sequence because it took place at the same segment already ruptured by the M_w 7.8–7.9 1942 earthquake[4,5]. All events of the sequence occurred at the megathrust where the oceanic Nazca Plate subducts below the North Andean Sliver[9–15] (NAS), a forearc domain moving 8–11 mm yr^{-1} northeastward with respect to the stable part of the South America Plate[12–14]. Owing to this partitioning, the relative Nazca/NAS motion is ~85% of the Nazca/South America Plate convergence rate[12,16], leading to a maximum slip deficit of 47 mm to accumulate every year at the megathrust. Global Positioning System (GPS) measurements made in the years preceding the 2016 event demonstrate rapid strain accumulation, with spatially heterogeneous interseismic coupling, mainly confined within the shallowest 35 km of the megathrust[12,17] (Fig. 1).

Rupture model of the 2016 M_w 7.8 Pedernales earthquake

The rupture of the 16 April 2016 earthquake could be accurately observed by local seismological and geodetic data (Fig. 2 and Supplementary Figs 1–5). At the coastline, high-rate GPS (HRGPS) recorded dynamic displacements reaching 2 m and accelerometer data showed peak ground accelerations exceeding 1g (ref. 18). From an inversion of near-field high-rate and static GPS, accelerometer, interferometric synthetic aperture radar (InSAR) and global broadband seismometer data, we find that the 2016 Pedernales earthquake ruptured a 100-km-long segment of the megathrust (Figs 3 and 4 and Methods). One to six metres of seismic slip occurred within a north–south trending 40 km narrow strip at the megathrust between depths of 15 and 30 km. Our model predicts little vertical displacements offshore, consistent with the absence of noticeable tsunami wave following the earthquake and the small signal observed at three DART buoys in the Pacific Ocean (Supplementary Fig. 6). After a slow moment release during the first 5 s, the rupture propagated southward at an average velocity of 2.3 km s^{-1} and involved the successive rupture of two distinct adjacent asperities (Fig. 3). The second 40 × 40 km^2 asperity broke over a short time span of ~10 s with slip exceeding 5 m, contributing to more than half (2.8×10^{20} Nm, M_w 7.6) of the total moment release (5.4×10^{20} Nm, M_w 7.8). This part of the rupture, located at ~20 km depth right below the populated coastline, correlates with the extensive damage reported from Pedernales to Canoa (Fig. 1). In addition, ground motion data (Fig. 3) and relative source time functions (Supplementary Fig. 7) highlight a southward directivity of the rupture, consistent with the severe damage observed in cities located south of the rupture, such as Manta and Portoviejo[18]. Aside from the local ground response and poor building constructions, our model shows that the rupture properties played a key role in the observed damage.

[1]Université Côte d'Azur, IRD, CNRS, Observatoire de la Côte d'Azur, Geoazur, F06560 Valbonne, France. [2]Instituto Geofísico, Escuela Politécnica Nacional, 2759 Quito, Ecuador. [3]Institut de Physique du globe de Paris, Sorbonne Paris Cité, Université Paris Diderot, UMR 7154 CNRS, F75005 Paris, France. [4]Sorbonne Universités, UPMC Université Paris 06, CNRS, Institut des Sciences de la Terre de Paris (ISTeP), F75005 Paris, France. [5]Instituto Geográfico Militar, 2435 Quito, Ecuador. [6]Servicio Geológico Colombiano, GNSS GeoRED Project, Center for Processing and Analysis of Geodetic Data, Bogotá, Colombia. *e-mail: nocquet@geoazur.unice.fr

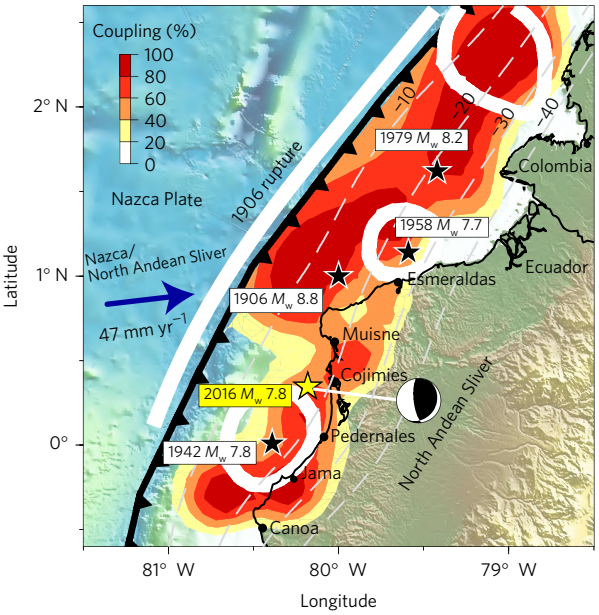

Figure 1 | Previous large earthquakes and interseismic coupling map along the central Ecuador–southern Colombia subduction zone. The black line with triangles indicates the location of the trench. Black stars indicate locations of epicentres of twentieth-century large earthquakes. The thick white lines delimit the area of major moment release for the earthquakes[5], whereas the white line following the trench shows the proposed rupture extent for the great M_w 8.8 earthquake of 1906[2]. The epicentre (yellow star, this study) and focal mechanism of the 2016 April 16 Pedernales earthquake are shown. The colour scale in the top-left corner indicates the interseismic spatial coupling derived from 1994–2013 GPS measurements. Dashed grey lines are depth contours of the subduction interface every 10 km (ref. 41).

Strain budget

Figure 4 shows a remarkable spatial correlation between the coseismic slip distribution and interseismic coupling models. The rupture only marginally propagated into low (<20%) interseismic coupling areas while larger seismic slip (>2 m) occurred at areas of higher (>60%) coupling. This correlation, already observed for recent earthquakes[19,20], is consistent with a model where the subduction interface is composed of discrete seismic asperities persisting during the interseismic period and separated by aseismic weak zones[2]. The 2016 rupture area encompasses proposed epicentre locations for the M_w 7.8–7.9 1942 earthquake[4,5,21] (Fig. 4). In the Methods, we show that, despite the uncertainties inherent to the scarcity of records in 1942, the available information concurs with a large overlap between the 2016 and 1942 earthquake slip distributions as proposed in ref. 8. Under this assumption, we first note that the ~6 m of peak seismic slip largely exceeds the 3.5 m slip deficit accumulated since 1942 assuming a full coupling. Overshoot has been observed for several recent earthquakes[22–25] and is usually attributed either to the dynamic of the rupture[22,26] or to the fact that the previous earthquake did not entirely reset the slip deficit[27,28]. Here, integrated at the scale of the 2016 entire rupture zone, we find that the slip during the 2016 earthquake exceeds by 30 to 60% the slip deficit estimated from the interseismic coupling models extrapolated over the 1942–2016 period, therefore favouring the latter explanation. For the 1906–1942 period, the 1942 earthquake[5] had a moment ($M_0 = 6–8 \times 10^{20}$ Nm, M_w 7.8–7.9) three to five times larger than the moment deficit accumulated over 36 years at the present-day rate. We conclude that the seismic rate at the Pedernales segment is not consistent with the idea of successive (1906, 1942, 2016) ruptures of the same persistent asperity, releasing the slip and moment deficit accumulated since the previous earthquake. Although we acknowledge potentially large uncertainties in interseismic coupling models close to the trench where GPS data provide low constraints (see Methods and Supplementary Fig. 10) or the possibility of temporal variations in strain accumulation[29,30], similar calculations carried out at many subduction segments elsewhere systematically led to the conclusion of earthquake moments smaller than the moment deficit estimated from interseismic coupling GPS-based models[19,20,31]. Such a result is expected because afterslip following large earthquakes[32], episodic slow slip events or moderate seismicity[20] all contribute to release a fraction of the accumulated strain. The 2016 earthquake appears to be abnormally large compared with the moment balance derived at other subduction zones. A similar conclusion also holds if one considers the alternative hypothesis whereby the 1942 and 2016 earthquakes had close but different main slip areas. As the 1942 earthquake slip distribution is unknown, we conservatively assume that it released most of its moment in an area of the interface comprised between latitude 0.5° S–0.5° N along strike and from the trench to 40 km depth. We find that the selected area accumulates a moment deficit of $8 \pm 1.5 \times 10^{18}$ Nm every year (see Methods). This value is equivalent for the 1906–1942 period to only 30% to 60% of the moment released by the 1942 earthquake, or 50% to a maximum of 90% of the moment released by the 1942 and 2016 earthquakes together for the 1906–2016 period. The moment budget for the other segments of the Ecuador–Colombia subduction zones ruptured during the twentieth century makes an even stronger case. Assuming a full coupling over their respective rupture areas, we find that the 1958 M_w 7.7 northern Ecuador earthquake[5] had a seismic moment exceeding by 50% to 180% the moment accumulated since 1906. For the 1979 M_w 8.2 southern Colombia earthquake[2,5], the seismic moment is at least 70% larger than the accumulated moment since 1906 (see Methods). We discard errors in the plate motion rate as a potential bias of our calculations. Indeed, a direct estimate using the GPS sites in the Galapagos Islands located ~1,000 km offshore in front of the Ecuador margin indicates a Nazca/NAS convergence rate of 47 mm yr^{-1}. The NAS kinematics is derived from GPS measurements distributed over a large area from latitude 3° S to 4.6° N with negligible internal deformation and is consistent with Holocene slip rates at continental faults accommodating its motion[12]. Hence, the uncertainty of the slip rate at the megathrust is at most a few millimetres per year, too small to explain the discrepancy in the moment budgets found here.

Earthquake supercycle

In simple models of the earthquake cycle, large and great earthquakes release the elastic strain accumulated during the previous interseismic period at highly locked asperities, resetting the slip and moment deficit. The moment balance during the Ecuador–Colombia seismic sequence challenges this view. At the Pedernales segment, regardless of whether the 1942 earthquake had a large overlap with the 2016 rupture, the 1942 and 2016 earthquakes correspond to a release of a moment deficit accumulated over a time window longer than 110 years. A simple explanation might be that the 1906 earthquake did not release all strain accumulated before it, and possibly did not even rupture the areas where the 1942 and 2016 earthquakes occurred. This would be consistent with smaller magnitudes proposed for this great earthquake[7,8]. Even so, both peak and averaged slips during the 2016 event indicate that significant residual slip deficit persisted after the 1942 earthquake. In the northern part of the 1906 earthquake area, where overlap with the 1958 and 1979 earthquakes is less doubtful, the moment released by the earthquakes exceeds even more clearly the strain accumulated since 1906.

The high rate of seismicity observed since 1906 contrasts with the lack of historical records of large earthquakes in coastal Ecuador

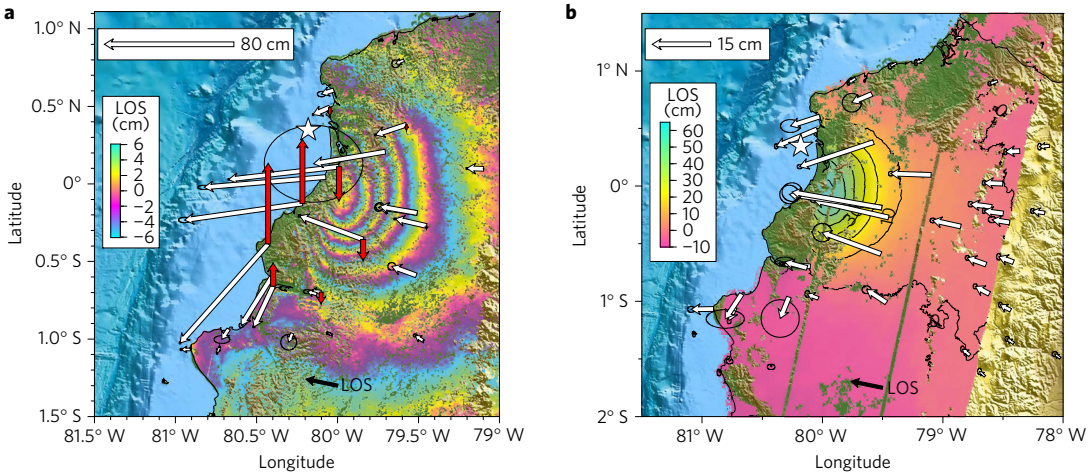

Figure 2 | Coseismic static displacements from GPS and InSAR. a, Near-field data. White and red arrows show horizontal and vertical GPS displacements respectively. Line-of-sight (LOS) displacement for the wrapped ALOS-2 descending interferogram (1 April 2016–29 April 2016) with one fringe every 12.125 cm is shown using the colour scale shown on the left. The LOS vector is indicated by the black arrow. Positive displacement corresponds to motion away from the satellite. The white star shows the epicentre location from this study. **b**, Intermediate and far-field data. White arrows show horizontal displacements. The unwrapped Sentinel-1 descending interferogram (12 April 2016–24 April 2016) is shown using the colour scale shown on the left of the figure.

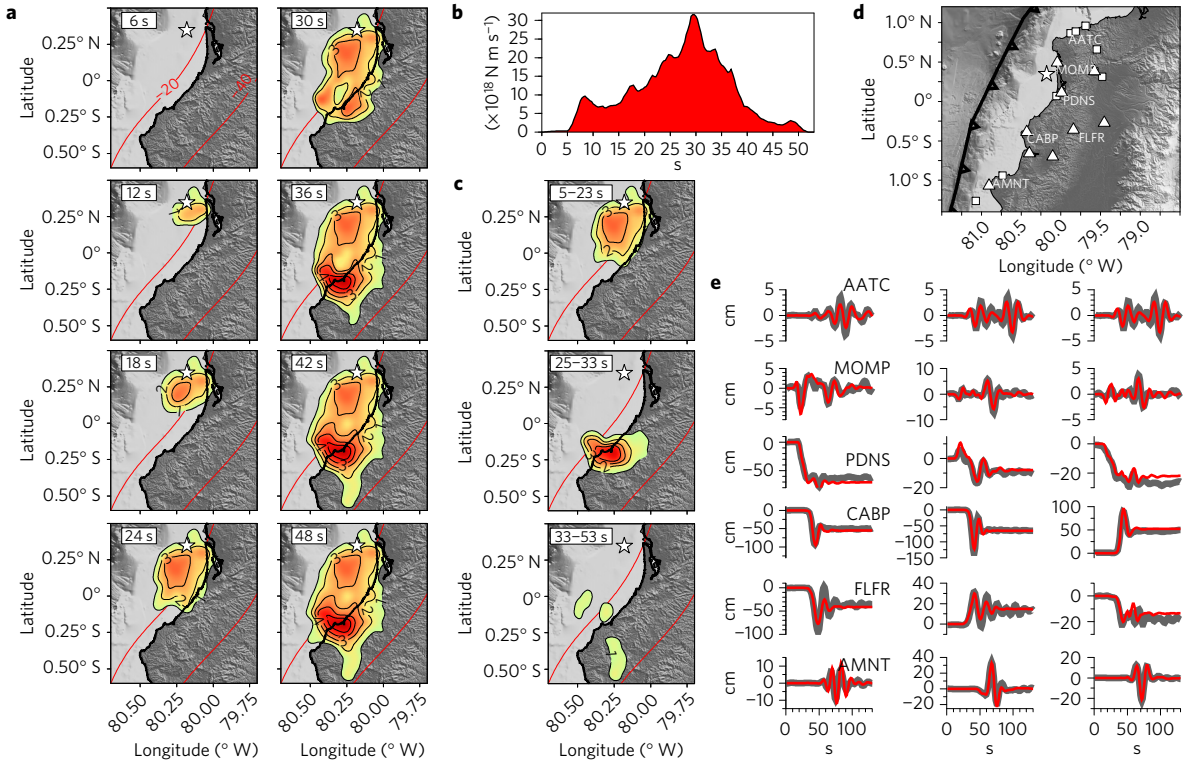

Figure 3 | Time evolution of the rupture and fit to HRGPS and accelerometer data. a, Snapshots of cumulated slip every 6 s, colour coded (same as Fig. 4a) and with contour intervals every metre. Red lines are depth contours of the subduction interface every 20 km (ref. 41). **b**, Source time function. **c**, Selected snapshots showing the three main phases of the rupture during the 5–23, 25–33 and 33–53 s time windows. These snapshots show the southward propagation of the rupture and the main moment release occurring between 25 and 33 s during the rupture of the second asperity. **d**, Location map of HRGPS (triangles) and accelerometer (squares) data used in the study. **e**, Observed (black lines) and modelled (red lines) HRGPS time series and integrated accelerograms for the east (left), north (middle) and up (right) components. The displacement scale is in centimetres and time is in seconds with reference to the earthquake origin time. Data and synthetics are low-pass-filtered below 0.08 Hz and static offsets are kept for the closest HRGPS stations (PDNS, CABP, FLFR). Higher amplitudes and a simpler signal recorded at AMNT compared with AATC highlight the southward propagation and resulting southward directivity.

before the twentieth century[15]. Cities such as Portoviejo and Manta were founded during the sixteenth century and reported intensity III damage for the 1797 M7.5–7.9 Riobamba crustal earthquake, located 230 km inland[33]. Both cities were heavily damaged during both the 1942 and 2016 earthquakes[18,34]. There is only a remote probability that an earthquake similar to the 2016 event would have hit them every century or so without leaving any historical account. We therefore propose that the Ecuador–Colombia subduction zone

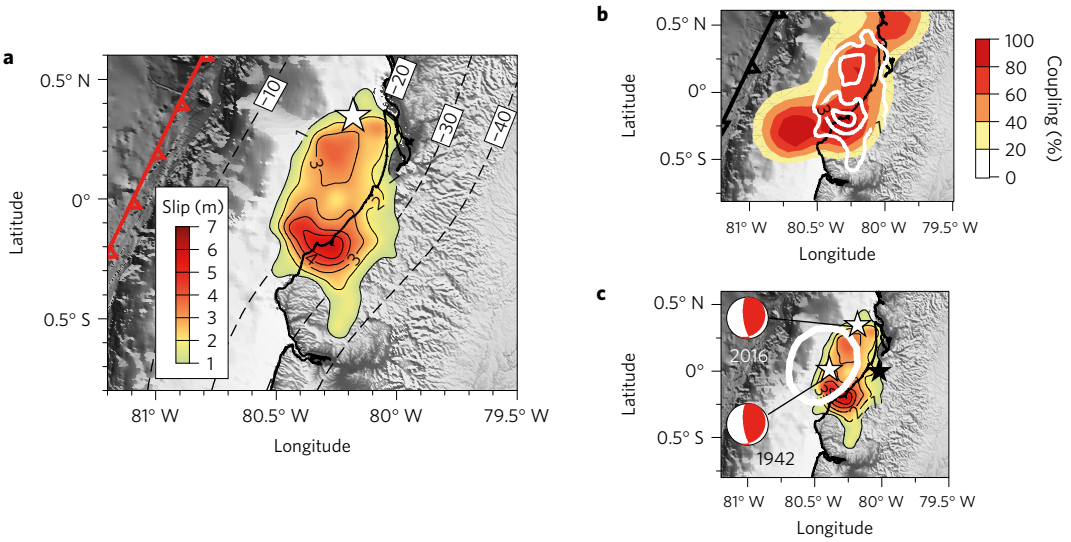

Figure 4 | Spatial slip distribution of the 2016 Pedernales earthquake. a, Green to red colours show extent and amount of coseismic slip (scale from 1 to 7 m) with contour intervals every metre. The white star shows the epicentre location from this study (longitude 80.17° W, latitude 0.35° N). Dashed black lines are depth contours of the subduction interface every 10 km (ref. 41). **b**, Interseismic spatial coupling map as in Fig. 1 together with the slip contours for 1, 3 and 5 m. **c**, Slip distribution with the main area of moment release for the 1942 M_w 7.8–7.9 earthquake[5] superimposed. Focal mechanisms for the 1942[5] and 2016 earthquakes are shown with their respective epicentres (white stars). The black star indicates the relocation of the 1942 epicentre from ISC-GEM[21].

illustrates in the present time a fault behaviour predicted by physical models that include spatial variation of fault friction[35] and identified by palaeoseismological studies[36–39], showing temporally clustered earthquakes separated by periods of seismic quiescence. A recent marine palaeoseismology study at the Ecuadorian margin further supports this view as earthquake-triggered deposits show 1906-like turbidites ~600 years ago, followed by a cluster of events with recurrence time of 40–70 years and then a ~300 years quiescence period preceding the twentieth-century sequence[40].

Seismic hazard assessment models commonly assume that the probability of occurrence of a large earthquake ($7 < M < 8$) in the decades following a great earthquake ($M \geq 8.5$) is reduced locally, because of the time required to reload the fault. As several subduction segments are now in the wake of a great earthquake, the lesson learned from the Ecuador–Colombia subduction zone is that a great earthquake can also have the opposite effect of initiating a phase of enhanced seismic release, with large earthquakes occurring more frequently than during the centuries prior to the great earthquake.

Methods

Methods, including statements of data availability and any associated accession codes and references, are available in the online version of this paper.

Received 27 September 2016; accepted 23 November 2016; published online 26 December 2016

References

1. Kelleher, J. A. Rupture zones of large South American earthquakes and some predictions. *J. Geophys. Res.* **77,** 2087–2103 (1972).
2. Kanamori, H. & McNally, K. Variable rupture mode of the subduction zone along the Ecuador-Colombia coast. *Bull. Seismol. Soc. Am.* **72,** 1241–1253 (1982).
3. Beck, S. L. & Ruff, L. J. The rupture process of the Great 1979 Colombia Earthquake: evidence for the asperity model. *J. Geophys. Res. Solid Earth* **89,** 9281–9291 (1984).
4. Mendoza, C. & Dewey, J. W. Seismicity associated with the great Colombia-Ecuador earthquakes of 1942, 1958 and 1979: implications for barrier models of earthquake rupture. *Bull. Seismol. Soc. Am.* **74,** 577–593 (1984).
5. Swenson, J. L. & Beck, S. L. Historical 1942 Ecuador and 1942 Peru subduction earthquakes, and earthquake cycles along Colombia-Ecuador and Peru subduction segments. *Pure Appl. Geophys.* **146,** 67–101 (1996).
6. Abe, K. Size of great earthquakes of 1837–1974 inferred from tsunami data. *J. Geophys. Res.* **84,** 1561–1568 (1979).
7. Okal, E. A. Use of the mantle magnitude M_m for the reassessment of the moment of historical earthquakes. *Pure Appl. Geophys.* **139,** 17–57 (1992).
8. Ye, L. *et al*. The 16 April 2016, M_w 7.8 (Ms 7.5) Ecuador earthquake: a quasi-repeat of the 1942 M_s 7.5 earthquake and partial re-rupture of the 1906 M_s 8.6 Colombia–Ecuador earthquake. *Earth Planet. Sci. Lett.* **454,** 248–258 (2016).
9. Pennington, W. Subduction of the Eastern Panama Basin and seismotectonics of northwestern South America. *J. Geophys. Res. Solid Earth* **86,** 10753–10770 (1981).
10. Trenkamp, R., Kellogg, J. N., Freymueller, J. T. & Mora, H. P. Wide plate margin deformation, southern Central America and northwestern South America, CASA GPS observations. *J. South Am. Earth Sci.* **15,** 157–171 (2002).
11. White, S. M., Trenkamp, R. & Kellogg, J. N. Recent crustal deformation and the earthquake cycle along the Ecuador-Colombia subduction zone. *Earth Planet. Sci. Lett.* **216,** 231–242 (2003).
12. Nocquet, J.-M. *et al*. Motion of continental slivers and creeping subduction in the northern Andes. *Nat. Geosci.* **7,** 287–292 (2014).
13. Nocquet, J.-M. *et al*. Addendum: motion of continental slivers and creeping subduction in the northern Andes. *Nat. Geosci.* **7,** 612 (2014).
14. Alvarado, A. *et al*. Partitioning of oblique convergence in the Northern Andes subduction zone: migration history and the present-day boundary of the North Andean Sliver in Ecuador. *Tectonics* **35,** 1048–1065 (2016).
15. Yepes, H. *et al*. A new view for the geodynamics of Ecuador: implication in seismogenic source definition and seismic hazard assessment. *Tectonics* **35,** 1249–1279 (2016).
16. Kendrick, E. *et al*. The Nazca–South America Euler vector and its rate of change. *J. South Am. Earth Sci.* **16,** 125–131 (2003).
17. Chlieh, M. *et al*. Distribution of discrete seismic asperities and aseismic slip along the Ecuadorian megathrust. *Earth Planet. Sci. Lett.* **400,** 292–301 (2014).
18. http://www.igepn.edu.ec/eq20160416-home
19. Moreno, M., Rosenau, M. & Oncken, O. 2010 Maule earthquake slip correlates with pre-seismic locking of Andean subduction zone. *Nature* **467,** 198–202 (2010).
20. Protti, M. *et al*. Nicoya earthquake rupture anticipated by geodetic measurement of the locked plate interface. *Nat. Geosci.* **7,** 6–10 (2013).
21. Storchak, D. A. *et al*. The ISC-GEM Global Instrumental Earthquake Catalogue (1900–2009): introduction. *Phys. Earth Planet. Inter.* **239,** 48–63 (2015).
22. Ide, S., Baltay, A. & Beroza, G. C. Shallow dynamic overshoot and energetic deep rupture in the 2011 M_w 9.0 Tohoku-Oki earthquake. *Science* **332,** 1426–1429 (2011).

23. Moreno, M. *et al*. Toward understanding tectonic control on the M_w 8.8 2010 Maule Chile earthquake. *Earth Planet. Sci. Lett.* **321–322,** 152–165 (2012).
24. Vallée, M. & Satriano, C. Ten year recurrence time between two major earthquakes affecting the same fault segment. *Geophys. Res. Lett.* **41,** 2312–2318 (2014).
25. Yin, J., Yang, H., Yao, H. & Weng, H. Coseismic radiation and stress drop during the 2015 M_w 8.3 Illapel, Chile megathrust earthquake. *Geophys. Res. Lett.* **43,** 1520–1528 (2016).
26. Ben-Zion, Y. & Rice, J. R. Dynamic simulations of slip on a smooth fault in an elastic solid. *J. Geophys. Res. Solid Earth* **102,** 17771–17784 (1997).
27. Cisternas, M. *et al*. Predecessors of the giant 1960 Chile earthquake. *Nature* **437,** 404–407 (2005).
28. Yagi, Y. & Fukahata, Y. Rupture process of the 2011 Tohoku-oki earthquake and absolute elastic strain release. *Geophys. Res. Lett.* **38,** L19307 (2011).
29. Perfettini, H. & Avouac, J.-P. Stress transfer and strain rate variations during the seismic cycle. *J. Geophys. Res. Solid Earth* **109,** B06402 (2004).
30. Mavrommatis, A. P., Segall, P. & Johnson, K. M. A decadal-scale deformation transient prior to the 2011 M_w 9.0 Tohoku-oki earthquake. *Geophys. Res. Lett.* **41,** 4486–4494 (2014).
31. Scholz, C. H. & Campos, J. The seismic coupling of subduction zones revisited. *J. Geophys. Res. Solid Earth* **117,** B05310 (2012).
32. Bürgmann, R. *et al*. Interseismic coupling and asperity distribution along the Kamchatka subduction zone. *J. Geophys. Res.* **110,** B07405 (2005).
33. Beauval, C. *et al*. Locations and magnitudes of historical earthquakes in the Sierra of Ecuador (1587–1996). *Geophys. J. Int.* **181,** 1613–1633 (2010).
34. Beauval, C. *et al*. An earthquake catalog for seismic hazard assessment in Ecuador. *Bull. Seismol. Soc. Am.* **103,** 773–786 (2013).
35. Kaneko, Y., Avouac, J.-P. & Lapusta, N. Towards inferring earthquake patterns from geodetic observations of interseismic coupling. *Nat. Geosci.* **3,** 363–369 (2010).
36. Sieh, K. *et al*. Earthquake supercycles inferred from sea-level changes recorded in the corals of West Sumatra. *Science* **322,** 1674–1678 (2008).
37. Weldon, R., Scharer, K., Fumal, T. & Biasi, G. Wrightwood and the earthquake cycle: what a long recurrence record tells us about how faults work. *Geol. Soc. Am. Today* **14,** 4–10 (2004).
38. Schlagenhauf, A. *et al*. Earthquake supercycles in Central Italy, inferred from 36Cl exposure dating. *Earth Planet. Sci. Lett.* **307,** 487–500 (2011).
39. Goldfinger, C., Ikeda, Y., Yeats, R. S. & Ren, J. Superquakes and supercycles. *Seismol. Res. Lett.* **84,** 24–32 (2013).
40. Migeon, S. *et al*. Earthquake-triggered deposits in the subduction trench of the North Ecuador/South Colombia margin and their implication for paleoseismology. *Mar. Geol.* http://dx.doi.org/10.1016/j.margeo.2016.09.008 (2016).
41. Hayes, G. P., Wald, D. J. & Johnson, R. L. Slab1.0: a three-dimensional model of global subduction zone geometries. *J. Geophys. Res. Solid Earth* **117,** B01302 (2012).

Acknowledgements

This work has been supported by the Institut de Recherche pour le Développement of France (IRD) and the Instituto Geofísico, Escuela Politécnica Nacional (IGEPN), Quito, Ecuador in the frame of the Joint International Laboratory 'Earthquakes and Volcanoes in the Northern Andes' (grant IRD 303759/00). Previous funding from the Agence Nationale de la Recherche of France (grant ANR-07-BLAN-0143-01), Programme National de Télédétection Spatiale (grant PNTS-2015-09), SENESCYT (grant Fortalecimiento del Instituto Geofísico) and SENPLADES (grant Generación de Capacidades para la Difusión de Alertas Tempranas) from Ecuador is acknowledged. We thank the Instituto Geográfico Militar (IGM) and the OCP from Ecuador, and the Servicio Geológico Colombiano, Proyecto GeoRED from Colombia for the use of their data. We are grateful to the global broadband seismic networks belonging to the FDSN (in particular IRIS and GEOSCOPE) and IGS contributors for free access to their broadband seismic and GPS data. Support from the ANR JCJ EPOST (grant ANR-14-CE03-0002) and the IRD office in Ecuador during the analysis and the post-earthquake survey is acknowledged. Finally, we acknowledge M. Ruiz and A. Alvarado from IGEPN for the logistic support during the weeks following the earthquake and G. Ponce for her help with the seismological data.

Author contributions

J.-M.N. coordinated the work and wrote the paper with F.R., M.V., R.G. and H.Y. P.A.M., A.S. and P.C. edited the paper. M.V. and B.D. performed the kinematic slip inversion. R.G. carried out InSAR analysis. D.F., S.H. and B.D. determined the epicentre location. A.L. and J.-C.S. performed the accelerometer data analysis. A.S. carried out the tsunami analysis. J.-M.N., F.R., P.J. and D.C. performed GPS analysis. Y.F., P.J., M.R., P.A.M., J.-M.N., F.R. and M.V. maintained the geodesy and seismological networks since 2008. P.J., F.R., P.A.M., D.C., H.M. and J.-M.N. carried out field work to collect the data after the earthquake. J.G., L.M. and P.C. contributed with logistic support.

Additional information

Supplementary information is available in the online version of the paper. Reprints and permissions information is available online at www.nature.com/reprints. Correspondence and requests for materials should be addressed to J.-M.N.

Competing financial interests

The authors declare no competing financial interests.

Methods

Geodetic data. We analyse the GPS data using the GAMIT/GLOBK v10.6 software[42], using the strategy described in ref. 12. For continuous GPS sites[43] (CGPS), the coseismic static displacements are derived from the difference between the position obtained the day following the earthquake (17 April 2016) and the position before the earthquake averaged over 3 days. Campaign GPS sites were measured 3 to 14 days after the earthquake. We account for postseismic displacements at CGPS sites by interpolating the postseismic displacement observed at the nearest CGPS sites, subtract the obtained value and conservatively add an uncertainty corresponding to 30% of the interpolated postseismic displacement. We use the TRACK code[42] to process 1 sample-per-second data, with respect to a reference site located ~400 km east from the rupture, ensuring no temporal overlaps of the seismic waves. We use SAR data from the C-band Sentinel-1 (European Space Agency, wavelength 5.55 cm) and L-band ALOS-2 (Japanese Aerospace Exploration Agency, wavelength 24.25 cm) to determine the coseismic line-of-sight displacement inland. Sentinel-1 wide-swath interferograms (IW mode) are computed using a modified version[44,45] of ROI_ PAC software[46], available at https://github.com/RaphaelGrandin/ROI_PAC-Sentinel1. ALOS-2 wide-swath interferograms (WD1 mode) are computed using GMTSAR software[47]. We process two Sentinel-1 interferograms from the ascending (29 March 2016–22 April 2016) and descending (12 April 2016–24 April 2016) passes, and one ALOS-2 interferogram on the descending pass (1 April 2016–29 April 2016). The topographic phase component is corrected using SRTM DEM[48]. An adaptive filter[49] is applied prior to unwrapping using the branch-cut algorithm[50] manually corrected against unwrapping errors. Stratified atmospheric delays evident in Sentinel-1 interferograms are corrected empirically by computing a quadratic phase–elevation relationship away from the deformation zone for elevations higher than 500 m a.s.l. A regional north–south trend in the ALOS-2 interferogram, probably due to ionospheric effects and/or orbital errors, is corrected empirically by computing a first-order polynomial surface away from the deformation zone. Both descending interferograms from Sentinel-1 and ALOS-2 show an elliptical fringe pattern with a maximum ~65 cm ground motion away from the satellite, consistent with subsidence and trenchward horizontal motion above the base of the rupture zone. Due to longer time span and lower coherence of C-band in vegetated lowland areas, the Sentinel-1 ascending interferogram is insufficiently coherent to warrant reliable phase unwrapping in the area of maximum deformation and was not used in the inversion.

Rupture kinematic inversion methods. The rupture kinematic inversion includes five data sets: HRGPS, static GPS, accelerograms (Supplementary Fig. 1), InSAR, and body waves at the global scale. We selected GPS displacements with magnitude larger than 1 cm and within 200 km from the epicentre. ALOS-2 and Sentinel-1 interferograms have been down-sampled according to the local deformation gradient. The three components in displacement from eight high-rate GPS and from ten accelerometers were band-pass-filtered between 0.015 Hz and 0.08 Hz, except when the low-frequency noise in the accelerometers required increasing the lower limit (sometimes up to 0.04 Hz). The selected HRGPS and accelerometer data ensure a homogeneous sampling of the area close to the earthquake. At the global scale, we used 15 P-wave and 10 SH-wave broadband records from the FDSN (Federation of Digital Seismograph Networks) with different azimuthal coverage and radiation pattern. All waveforms were band-pass-filtered in displacement between 0.005 Hz and 0.25 Hz.

All data sets were simultaneously inverted using the method of ref. 51, recently adapted and applied to the study of megathrust earthquakes[52,53]. The model geometry consists of a single 150-km-long and 80-km-wide fault segment, divided into 120 square subfaults (Supplementary Fig. 1). The chosen geometry with a constant strike (26°) and dip (23°) is consistent with the focal mechanism derived from teleseismic data (Global CMT[54], SCARDEC[55]), and the SLAB1.0 (ref. 41) model close to the coast. With significant slip offshore at shallow depth having been ruled out by initial inversions, more complex geometry including a shallower dip close to the trench was not required. The fault model is embedded in a stratified crustal structure, determined by modelling the seismic waveforms of a M_w 5.2 earthquake (25 November 2010). This approach ensures that the waveform complexity (up to 0.08 Hz) due to propagation effects will be accounted for in our inversion. Local synthetic seismograms (HRGPS and accelerometric data), teleseismic P and SH displacements, and synthetic static displacements (static GPS and InSAR) were computed using the discrete wavenumber method[56], the reciprocity approach[57], and the Green's function approach of ref. 58 respectively, all consistently calculated using the stratified medium (Supplementary Table 3). Earthquake origin time and hypocentre location have been determined in the same crustal model by combining the arrival times and the first motion directions recorded at 8 accelerometers. The epicentre is found at longitude 81.17° W, latitude 0.35° N, depth 17 km. The earthquake origin time is 16 April 2016, 23 h 58 m 33 s. The continuous rupture is approximated by a summation of point sources at the centre of each subfault. For each point source, the local source time function is represented by two mutually overlapping isosceles triangular functions of duration equal to 5 s. For each of the 120 subfaults, the parameters to be inverted are the slip onset time, the rake angle, and the amplitudes of the two triangular functions. A nonlinear inversion is performed using a simulated annealing optimization algorithm. The convergence criterion is based on the minimization of the root-mean-square data misfit, with a moment minimization constraint, and optional smoothing constraints on the coseismic slip, rupture velocity, and rake angle variations, used to penalize unnecessarily complex models.

Kinematic source model misfit. The model shown in Figs 3 and 4 corresponds to a kinematic fault slip inversion obtained by giving the same weight to static GPS, local ground motions (HRGPS & accelerometers), and teleseismic data while half of this weight is applied to InSAR in order account for potential postseismic displacement. Rupture velocity is constrained to be between 1 km s^{-1} and 3.3 km s^{-1} and rake can vary at ±25° around an average value of 122°. Small smoothing constraints on slip amplitude, rupture velocity, and rake angle, as well as a minimization constraint of the global moment, were applied. The agreement between model predictions and local ground motion (HRGPS and accelerometer data) is shown in Fig. 3 and in the Supplementary Fig. 2. For the GPS static coseismic displacements, the weighted root mean square of residuals is 8 mm, 6 mm and 12 mm for the east, north and up components respectively (Supplementary Fig. 4). For InSAR, the root mean square of residuals is 12 and 20 mm for Sentinel-1 and the ALOS-2 interferograms. Larger residuals, up to 5 cm for the ALOS-2 interferogram, are found near the coast (Supplementary Fig. 5), reflecting postseismic deformation between the date of the earthquake and the time of ALOS-2 acquisition (29 April 2016), but do not impact the model because of the smaller weight given to InSAR data compared with GPS near-field data.

Model validation from relative source time function and Tsunami data. As a first independent validation of the source model, we compare predictions from our model with broadband surface waves recorded at teleseismic stations. We adopt an empirical Green function (EGF) approach, using as EGF the M_w 6.7 aftershock (18 May 2016, 7 h 57). Relative source time functions (RSTFs) are obtained using a stabilized deconvolution technique[59], with four physical constraints on the RSTFs (causality, positivity, limited duration and equal area) imposed in the deconvolution process. Supplementary Fig. 7 shows the Love waves RSTFs, recorded at ten stations of the FDSN (filled curves), together with the RSTFs derived from our spatio-temporal model, considering a Love waves phase velocity equal to 4.5 km s^{-1}. Because variations of the surface-wave RSTFs as a function of station azimuth are strongly sensitive to horizontal properties of the rupture process, the similarity between observed and computed RSTFs is an independent validation of our source model. It confirms two of the main earthquake propagation characteristics: the southward rupture propagation, with an average rupture velocity of 2.3 km s^{-1}; and the spatio-temporal location of the dominant slip patch.

As a second independent validation, we use tsunami observations recorded at the three deep-ocean buoys from the National Oceanic and Atmospheric Administration (NOAA), being the closest from the rupture (buoys 32067, 32411 and 32413, Supplementary Fig. 6). The three buoys are located in different azimuths from the source, and are therefore sensitive to relatively different parts of the source. The first tsunami oscillation appears clearly at all stations, but the signals are of relatively small amplitude (1 cm at stations 32411 and 32413) compared with the noise level (0.3 to 0.5 cm). Since the low signal-to-noise ratio could induce a bias in the finite-fault slip inversion, we restrict our analysis to a forward prediction. We simulate the tsunami corresponding to our preferred finite-fault source model using a standard finite-difference numerical code implementing the classical nonlinear shallow-water theory[60]. The tsunami wave is generated assuming that the sea-bottom deformation caused by the earthquake is fully and instantaneously transmitted to the above water column. The bathymetry 'advection' effect[61], which is non-negligible near the trench[62], is taken into account. The simulation is run using the ETOPO1 1 arc-minute global relief model. Our tsunami simulation predicts very well the arrival time, magnitude and the main first wave oscillations at all three offshore stations (Supplementary Fig. 6). The timing of the first tsunami waves is directly related to the offshore extent of the rupture. Hence, these tsunami results support our preferred finite-fault slip model and also our interpretation that the rupture had a very limited offshore extension, explaining the absence of significant tsunami after the earthquake.

Overlap between the 1942 and 2016 rupture. We review the different observations available to discuss the overlap between the 1942 and 2016 rupture areas. With a thrust mechanism and shallow dip angle, the focal mechanism indicates that the 1942 event is a subduction interface event. Two hypocentre locations have been determined for this event[4,21]. Both are located within areas of significant (~1 m) slip during the 2016 earthquake (Fig. 4 and Supplementary Fig. 8). The proposed depths[4,21] (19.7, 20 km) and dip (preferred value of 20°)[5] are consistent with the SLAB1.0 (ref. 41) subduction interface geometry model for a location ~70 km from the trench and with a similar location to the 2016 earthquake determined from teleseismic data (depth 17 km, dip 19°–24°, http://www.emsc-csem.org/Earthquake/tensors.php?id=501158&id2=BIGQ7;INFO). Both

earthquakes did not generate significant tsunami suggesting that both did not induce very large vertical motion offshore. Both aftershock distributions show a very specific pattern with two stripes of higher density of earthquakes located at latitude 0.75° N and 0.2° S respectively (Supplementary Fig. 8), also active during the interseismic period[63]. Hence, the 2016 aftershock distribution does not directly outline the coseismic slip distribution, but rather stimulates areas prone to seismicity during the interseismic period. Although the 1942 aftershocks appear to be shallower on average, relocation of the largest events from the ISC-GEM[21] catalogue shifts them eastward by ∼20 km. Thus, within the uncertainties, the 1942 and 2016 earthquakes activated a similar area of aftershocks. Maximum intensity for the 1942 earthquake is found at an area extending from south of Pedernales to north of Manta[5]. It suggests that the seismic waves had stronger energy in that area as they also had for the 2016 earthquake. Although certainly not demonstrating the overlap, the similarity of the 1942 and 2016 intensity maps adds an observation favouring a similar location of both earthquakes. Finally, we compare seismograms for the 1942 and 2016 earthquakes recorded at the station DBN (Netherlands). In 1942, a Galitzin seismometer (dominant period of 25 s) clearly recorded the east component of the P wave[5]. DBN seismic station is now equipped by KNMI (Koninklijk Nederlands Meteorologisch Instituut) with a digital long-period instrument, operating in a broad frequency range that includes the frequency band of the Galitzin (http://rdsa.knmi.nl/dataportal). Supplementary Fig. 9a shows the 2016 earthquake east component, first deconvolved from the long-period modern sensor response and then reconvolved by the Galitzin response, so that both signals can be directly compared. The comparison confirms that the 2016 earthquake had a longer duration than the 1942 earthquake. The 2016 earthquake therefore cannot be considered as a strict repeat of the 1942 event. The comparison further supports a relatively short duration of 24 s for the 1942 earthquake, implying that most of the moment was released in the vicinity of the hypocentre[5]. However, there is a clear similarity of the waveforms when shifting the 1942 waveforms by about 15 s (Supplementary Fig. 9b) as also found in ref. 8. This indicates that the focal mechanism and depth of the 1942 and 2016 earthquakes are similar. Given the proposed location for the 1942 hypocentre and the observed time shift, the simplest explanation for the observed waveform similarity is that the 1942 rupture largely overlaps with the second patch of high slip found for the 2016 earthquake. To further test this hypothesis, we simulate the waveforms that would have been observed at DBN station for a virtual earthquake having exactly the same coseismic slip distribution as our solution for the 2016 earthquake, the same rupture velocity of 2.3 km s^{-1}, but that would have started (hypocentral location) 30 km south of the 2016 hypocentre. The isochrones shown every 5 s in the inset of Supplementary Fig. 9c indicate a rupture duration of 25–30 s for this virtual earthquake. Such a virtual earthquake is able to reproduce not only the duration of the signal at DBN for the 1942 earthquake, but also reproduces the main pattern of the waveform (Supplementary Fig. 9c). Although not ruling out that other rupture models could also reproduce the waveforms at DBN, this simulation argues for a very similar rupture area for both earthquakes. This comparison provides additional arguments relevant to the question of the overlap. Given its shorter duration, the 1942 earthquake probably had a bi-lateral propagation, and must have had a length between 50 and 100 km centred on the epicentre. Fitting such a length with no overlap with the 2016 coseismic slip distribution requires the rupture of the 1942 earthquake to be either located updip or downdip of the 2016 rupture. A downdip location would disagree with the intensity recorded in 1942, and would have implied a greater depth (∼40 km) contradicting the similarity of the waveforms. An updip location is also unlikely because of the 20° dip value, and because very shallow subduction earthquakes (depth <15 km) tend to have slower rupture velocity and longer source time function than average[64]. A 24 s duration is very short for a M_w 7.8 earthquake and argues against a shallow rupture. We conclude that, although the large overlap cannot be demonstrated in the absence of geodetic data, there is a very high probability that the 1942 and 2016 slip distributions largely overlap and rupture a common subset of locked asperities.

Interseismic spatial coupling, slip and moment deficit estimates. The interseismic coupling map is derived using the velocity field from ref. 12 augmented from two sites in southern Colombia provided by the Geological Service of Colombia and benefiting from data since 2011. The SLAB1.0 (ref. 41) subduction interface geometry between latitude 2° S and 4.6° N is discretized using 1,130 quasi-equilateral triangles of 10-km-long edges. Green's functions relating the unit slip in the Nazca Plate/NAS direction to horizontal displacements are calculated in a semi-infinite homogeneous elastic half-space[65]. We use the back-slip approach[66] and a Bayesian formalism in the linear case[67] to invert the slip at each individual subfault. In this approach, the regularization is imposed through a model covariance matrix C_m, reflecting the a priori knowledge with respect to an a priori model m_0. C_m simultaneously controls the smoothing and damping with respect to m_0. In our approach, C_m is taken as a decreasing exponential with a critical length L and weighted by a parameter σ with unit of mm yr^{-1}. The inversion uses the bounded least-square algorithm from ref. 68. This approach is used to explore the range of models allowed by the GPS data, by changing the a priori model m_0 from 0% (null coupling) to 100% (full coupling), σ the constraint to the a priori model from 3 to 50 mm yr^{-1} and a critical correlation distance L from 20 to 100 km. As a result, we obtain a probability density function (PDF) for the individual inverted slip or for a subset of them within a studied zone. The total slip for the 2016 earthquake mentioned in the text corresponds to the integral of slip over the rupture area defined as areas with at least 0.5 m of slip in our model. The expectation of the PDF and the associated uncertainties derived from the PDF are given at the 95% confidence level. When converted into moment deficit rate, we conservatively add an additional uncertainty equal to 10% of the estimated value to account for uncertainties in the rigidity module (3×10^{10} Pa was used). The inversion procedure is illustrated in Supplementary Fig. 10 for the Pedernales segment. For the 1958 northern Ecuador earthquake (M_w 7.7), we take a 50×50 km^2 rupture area[5] and a full coupling. The maximum moment deficit accumulated since 1906 is $\sim 1.9 \times 10^{20}$ Nm, much smaller than the seismic moment values of $2.8–5.2 \times 10^{20}$ Nm proposed for this earthquake[2,3]. For the 1979 southern Colombia earthquake (M_w 8.2), upper bound values of 240×70 km^2 for the rupture area[2,5] lead to a maximum moment deficit of 1.7×10^{21} Nm accumulated since 1906, also assuming a full coupling. This is again significantly smaller than the 2.9×10^{21} Nm estimated for the moment of the 1979 event[2].

Data availability. The raw accelerometric and GPS data from IGEPN and IRD are provided on request made at http://www.igepn.edu.ec/solicitud-de-datos. IGM GPS data are available at www.igm.gob.ec, subject to the policies of IGM. GPS data from the global GNSS network IGS are available at http://www.igs.org. Sentinel-1 data are publicly available from https://scihub.copernicus.eu, subject to the policy of the European Space Agency and Copernicus programme. Advanced Land Observing Satellite-2 (ALOS-2) data are available from the Japan Aerospace Exploration Agency subject to its policies. DART data are available at http://www.ndbc.noaa.gov. Global broadband seismological data are available from IRIS (https://www.iris.edu) and GEOSCOPE (http://geoscope.ipgp.fr/index.php/en).

References

42. Herring, T. A., King, R. W., Floyd, M. A. & McClusky, S. C. *GAMIT/GLOBK Reference Manual, 10.6* (MIT, 2015).
43. Mothes, P. A., Nocquet, J.-M. & Jarrín, P. Continuous GPS network operating throughout Ecuador. *EOS, Trans. Am. Geophys. Union* **94,** 229–231 (2013).
44. Grandin, R. Interferometric processing of SLC Sentinel-1 TOPS data. *Proc. 2015 ESA Fringe Workshop* European Space Agency Special Publication Vol. SP-731 (European Space Agency, 2015).
45. Grandin, R., Klein, E., Métois, M. & Vigny, C. Three-dimensional displacement field of the 2015 M_w 8.3 Illapel earthquake (Chile) from across- and along-track Sentinel-1 TOPS interferometry. *Geophys. Res. Lett.* **43,** 2552–2561 (2016).
46. Rosen, P. A., Hensley, S., Peltzer, G. & Simons, M. Updated repeat orbit interferometry package released. *EOS, Trans. Am. Geophys. Union* **85,** 47 (2004).
47. Sandwell, D., Mellors, R., Tong, X., Wei, M. & Wessel, P. Open radar interferometry software for mapping surface deformation. *EOS Trans. Am. Geophys. Union* **92,** 234 (2011).
48. Farr, T. & Kobrick, M. Shuttle radar topography mission produces a wealth of data. *EOS Trans. Am. Geophys. Union* **81,** 583–585 (2000).
49. Goldstein, R. M. & Werner, C. L. Radar interferogram filtering for geophysical applications. *Geophys. Res. Lett.* **25,** 4035–4038 (1998).
50. Goldstein, R. M., Zebker, H. A. & Werner, C. L. Satellite radar interferometry: two-dimensional phase unwrapping. *Radio Sci.* **23,** 713–720 (1988).
51. Delouis, B., Giardini, D., Lundgren, P. & Salichon, J. Joint inversion of InSAR, GPS, teleseismic, and strong-motion data for the spatial and temporal distribution of earthquake slip: application to the 1999 .Izmit mainshock. *Bull. Seismol. Soc. Am.* **92,** 278–299 (2002).
52. Bletery, Q. *et al*. A detailed source model for the M_w9.0 Tohoku-Oki earthquake reconciling geodesy, seismology, and tsunami records. *J. Geophys. Res. B* **119,** 7636–7653 (2014).
53. Grandin, R. *et al*. Rupture process of the $M_w = 7.9$ 2015 Gorkha earthquake (Nepal): insights into Himalayan megathrust segmentation. *Geophys. Res. Lett.* **42,** 8373–8382 (2015).
54. Ekström, G., Nettles, M. & Dziewoński, A. M. The global CMT project 2004–2010: centroid-moment tensors for 13,017 earthquakes. *Phys. Earth Planet. Inter.* **200–201,** 1–9 (2012).
55. Vallée, M., Charléty, J., Ferreira, A., Delouis, B. & Vergoz, J. SCARDEC: a new technique for the rapid determination of seismic moment magnitude, focal mechanism and source time functions for large earthquakes using body-wave deconvolution. *Geophys. J. Int.* **184,** 338–358 (2011).
56. Bouchon, M. A simple method to calculate Green's functions for elastic layered media. *Bull. Seismol. Soc. Am.* **71,** 959–971 (1981).
57. Bouchon, M. Teleseismic body wave radiation from a seismic source in a layered medium. *Geophys. J. Int.* **47,** 515–530 (1976).

58. Wang, R., Mart, F. L. & Roth, F. Computation of deformation induced by earthquakes in a multi-layered elastic crust — FORTRAN programs. **29,** 195–207 (2003).
59. Vallée, M. Stabilizing the empirical Green function analysis: development of the projected Landweber method. *Bull. Seismol. Soc. Am.* **94,** 394–409 (2004).
60. Heinrich, P., Schindele, F., Guibourg, S. & Ihmlé, P. F. Modeling of the February 1996 Peruvian Tsunami. *Geophys. Res. Lett.* **25,** 2687–2690 (1998).
61. Tanioka, Y. & Satake, K. Tsunami generation by horizontal displacement of ocean bottom. *Geophys. Res. Lett.* **23,** 861–864 (1996).
62. Bletery, Q., Sladen, A., Delouis, B. & Mattéo, L. Quantification of Tsunami bathymetry effect on finite fault slip inversion. *Pure Appl. Geophys.* **172,** 3655–3670 (2015).
63. Font, Y., Segovia, M., Vaca, S. & Theunissen, T. Seismicity patterns along the Ecuadorian subduction zone: new constraints from earthquake location in a 3-D a priori velocity model. *Geophys. J. Int.* **193,** 263–286 (2013).
64. Bilek, S. L. & Lay, T. Rigidity variations with depth along interplate megathrust faults in subduction zones. *Nature* **400,** 443–446 (1999).
65. Okada, Y. Internal deformation due to shear and tensile faults in a half-space. *Bull. Seismol. Soc. Am.* **82,** 1018–1040 (1992).
66. Savage, J. C. A dislocation model of strain accumulation and release at a subduction zone. *J. Geophys. Res.* **88,** 4984–4996 (1983).
67. Tarantola, A. *Inverse Problem Theory and Methods for Model Parameter Estimation* (SIAM, 2005).
68. Stark, P. & Parker, R. Bounded-variable least-squares: an algorithm and applications. *Comput. Stat.* **10,** 129–141 (1995).